Oxidation-dependent mechanical response of graphene oxide: Improving the reliability of atomistic modeling by *ab initio* machine learning simulations

Sara Shahbazi Fashtali [1,*] Pablo M. Piaggi [2,3] and Giuseppe Zollo [1]

[1] *Dipartimento di Scienze di Base e Applicate per l'Ingegneria, Sapienza University of Rome, Via A. Scarpa 14–16, 00161 Rome, Italy*

[2] *CIC nanoGUNE, Tolosa Hiribidea 76, 20018 Donostia-San Sebastián, Spain*

[3] *Ikerbasque, Basque Foundation for Science, 48013 Bilbao, Spain*

(Received 24 July 2026; accepted 5 October 2026; published 2 November 2026)

The mechanical response of graphene oxide (GO) is controlled by oxidation level and functional group composition, yet a clear atomic level picture remains ambiguous due to limitations of classical reactive force fields. Here, we develop a machine learning interatomic potential by fine-tuning a MACE foundation model on density functional theory data. We employ this potential to systematically investigate GO tensile behavior across oxidation levels of 10% to 40% and hydroxyl-to-epoxy (OH/O) ratios of 0 to 3. Our potential accurately reproduces the expected decrease in Young's modulus and ultimate tensile strength with increasing oxidation, correcting the overestimation and dispersion characteristic of ReaxFF predictions. In the elastic and plastic regimes, oxidation level dominates the mechanical response, while the functional group identity remains secondary. In the fracture regime, however, chemical composition becomes significant, controlling ductile/brittle behavior. In highly oxidized, hydroxyl-rich systems, stress relaxation via dehydration, not captured by reactive force fields, critically influences fracture behavior.

DOI: 10.1103/vwr6-mt41

I. INTRODUCTION

Graphene oxide (GO), which is obtained through the oxidation of graphite, has unique thermodynamic [1–4], mechanical [5–10], electronic [11], and optical properties [12] arising from the presence of oxygen-containing functional groups on the graphene lattice. These properties make GO a candidate for several technological applications, including GO papers [13], flexible electronics materials [14,15], supercapacitors for energy storage [16], drug-delivery carriers and biomedical platforms [17], tissue repair system [18] supercapacitors [19], and GO-reinforced construction materials [20].

In all these applications fields, the mechanical behavior of GO affects directly the reliability, durability, and service life of the relevant GO-based nanodevices. However, according to the recent literature, the structural and chemical properties of GO strongly depend on the synthesis method and material quality, which determine the oxidation level and the distribution of functional groups [21,22]. As a result, the oxidation value in GO can vary significantly, typically ranging between 15% and 40% [9,23–30], with a consequent spread of the experimental data. Due to this variability, GO can be regarded as a family of materials with diverse chemical compositions and structural configurations, rather than a single well-defined material.

This is particularly clear if we focus on the GO mechanical properties, given the substantial amount of experimental data available from studies performed on GO papers [8,31] and monolayer GO sheets using atomic force microscopy (AFM) [10] and combined contact-mode AFM with finite element modeling (FEM) [9]. While these experiments provide valuable insight into the mechanical behavior of GO, they offer limited control over the chemical composition and structural complexity of the material. Consequently, they cannot fully resolve the relationship between oxidation chemistry, atomic-scale structure, and mechanical response.

For this reason, atomistic simulations, such as molecular dynamics (MD), provide an essential complementary approach to systematically investigate the structural and mechanical properties of GO.

A large body of work has investigated the mechanical properties of GO using classical interatomic potentials, with the reactive force field (ReaxFF) [32] being one of the most widely used approaches [27,33–42]. However, several studies have reported limitations of ReaxFF, including the tendency to overestimate tensile strengths and the presence of significant noise in the stress-strain response of graphene-based systems [43,44]. The limitations of the above approach are the main cause of some controversial results reported for the effect of oxidation on key mechanical properties, such as Young's modulus (E) [40] and ultimate tensile stress (UTS) [38], which often do not exhibit clear or consistent trends.

In addition, the influence of functional groups is often clearly distinguishable only in extreme cases, such as

*Contact author: sara.shahbazifashtali@uniroma1.it

Published by the American Physical Society under the terms of the Creative Commons Attribution 4.0 International license. Further distribution of this work must maintain attribution to the author(s) and the published article's title, journal citation, and DOI.

systems containing exclusively epoxy or hydroxyl groups. For intermediate OH/O ratios, the mechanical response frequently becomes ambiguous, and the individual contributions of epoxy and hydroxyl groups to the deformation behavior are still a subject under debate [33,36]. Density functional theory (DFT) studies have also been performed to investigate the mechanical properties of GO. Although DFT returns some useful indications on the brittle or ductile behavior for, respectively, low and high oxidation levels [45,46], it offers only limited access to meaningful system sizes and sets of structural samples, thus making the exploration of multiple oxidation levels and functional-group ratios computationally intractable. Moreover, the computational workload required by DFT *ab initio* MD precludes any attempt to perform systematic stress-strain simulation campaign of GO systems at realistic thermodynamic conditions.

The recent introduction of DFT-based machine learning interatomic potentials is the breakthrough we need to bridge the gap between classical molecular dynamics and DFT calculations, making it possible to carry out large-scale molecular dynamics simulations with near-DFT accuracy.

Here, we characterize the mechanical response of GO using an *ad hoc* machine learning interatomic potential (MLIP), which allows us to probe previously inaccessible simulation time and length scales. We first fine-tuned a universal MLIP using DFT calculations based on the Perdew-Burke-Ernzerhof (PBE) [47] functional in order to describe with high accuracy the full deformation process of GO. Then, we apply our fine-tuned model, MACE-PBE-FT, to carry out uniaxial tensile tests simulations. Our simulations span a broad range of oxidation levels, from 10% to 40%, and epoxy to hydroxyl ratios from 0 to 3. The present DFT-driven results provide a marked improvement of the predictive capability of MD, with closer agreement with the known experimental results, relative to the current standard making use of the ReaxFF force field.

Moreover, we evidence the importance of dehydration phenomena as a concurrent stress-relief mechanism in hydroxyl rich GO. More broadly, our results show the improved predictive power of MLIP vs ReaxFF, and provide a key link between atomistic structure and mechanical properties of GO.

II. COMPUTATIONAL METHODS

A. Training of the machine learning potential

The MLIP, referred to as PBE-MACE-FT, was obtained by fine-tuning the MATPES-PBE-0 MACE foundation model [48] on a dataset of DFT-calculated GO configurations. The training was performed using both energies and forces, using weights 1.0 and 10.0 for the energy and force terms of the loss function, respectively. The model architecture consists of three interaction layers with 64 channels and a cutoff radius of 5.0 Å, with a maximum angular momentum of $L = 2$. Optimization was carried out using the Adam optimizer with a learning rate of 3×10^{-4} and a batch size of 4. An exponential moving average (EMA) of the model parameters was employed to improve training stability. Fine-tuning was performed for 100 epochs starting from the pretrained weights.

B. Density-functional theory calculations

DFT calculations were performed using the QUANTUM ESPRESSO package [49,50]. The PBE exchange-correlation functional [47] was employed. Ultrasoft pseudopotentials from the PSLibrary [51] were employed for C, O, and H atoms. Calculations were carried out using a plane-wave basis set with a kinetic energy cutoff of 90 Ry. The charge density cutoff was set to 360 Ry. Brillouin zone sampling was restricted to the Γ point. Electronic occupations were treated using Fermi-Dirac smearing with a smearing width of 0.001 Ry. The electronic self-consistent field (SCF) cycle was converged to a threshold of 10^{-8} Ry with a maximum of 1000 iterations. Wave functions were optimized using Davidson diagonalization and a mixing parameter of 0.3. All other parameters were set to their default values in QUANTUM ESPRESSO. No explicit dispersion correction was included in the PBE reference calculations.

C. Molecular dynamics simulations

The simulated systems were based on a graphene nanoribbon containing 968 atoms and dimensions of approximately $51 \times 42\,\text{Å}^2$. The edges along the x direction were passivated with hydrogen atoms, while periodic boundary conditions were applied in all three directions. GO structures were generated by introducing epoxy and hydroxyl functional groups randomly distributed on both sides of the GO monolayer following the Lerf-Klinowski (L-K) structural model of GO [52]. For each combination of oxidation level and OH/O ratio, one single generated random distribution of functional groups was considered. Therefore, the reported mechanical properties correspond to a single structure for each composition. The relatively large system size is expected to provide substantial self-averaging, as each structure contains a large number of local environments and functional group arrangements. Oxidation levels and hydroxyl-to-epoxy ratios, increased the total number of atoms depending on the functionalization.

Simulations using the PBE-MACE-FT potential were carried out within the Atomic Simulation Environment (ASE) framework [53], whereas simulations employing the classical force fields were performed using the Large-scale Atomic/Molecular Massively Parallel Simulator (LAMMPS) [54] with the ReaxFF potential parametrized for C-H-O systems [32] in GO nanoribbons and AIREBO [55] for graphene nanoribbons. In both simulation frameworks, the systems were first subjected to energy minimization followed by equilibration in the isothermal-isobaric (NPT) ensemble for 25 ps at a temperature of 300 K and zero applied pressure along the y direction. This step ensured structural relaxation and thermal equilibration of the nanoribbons prior to mechanical loading. After equilibration, uniaxial tensile deformation was applied along the y direction using a constant engineering strain rate of $1 \times 10^{-6}\,\text{fs}^{-1}$. During the deformation stage, the simulations were performed in the canonical (NVT) ensemble maintaining the temperature at 300 K. The deformation was continued until structural failure occurred in each system. Stress was computed from the virial expression and reported as engineering stress, obtained by dividing the virial tensor component along the loading direction

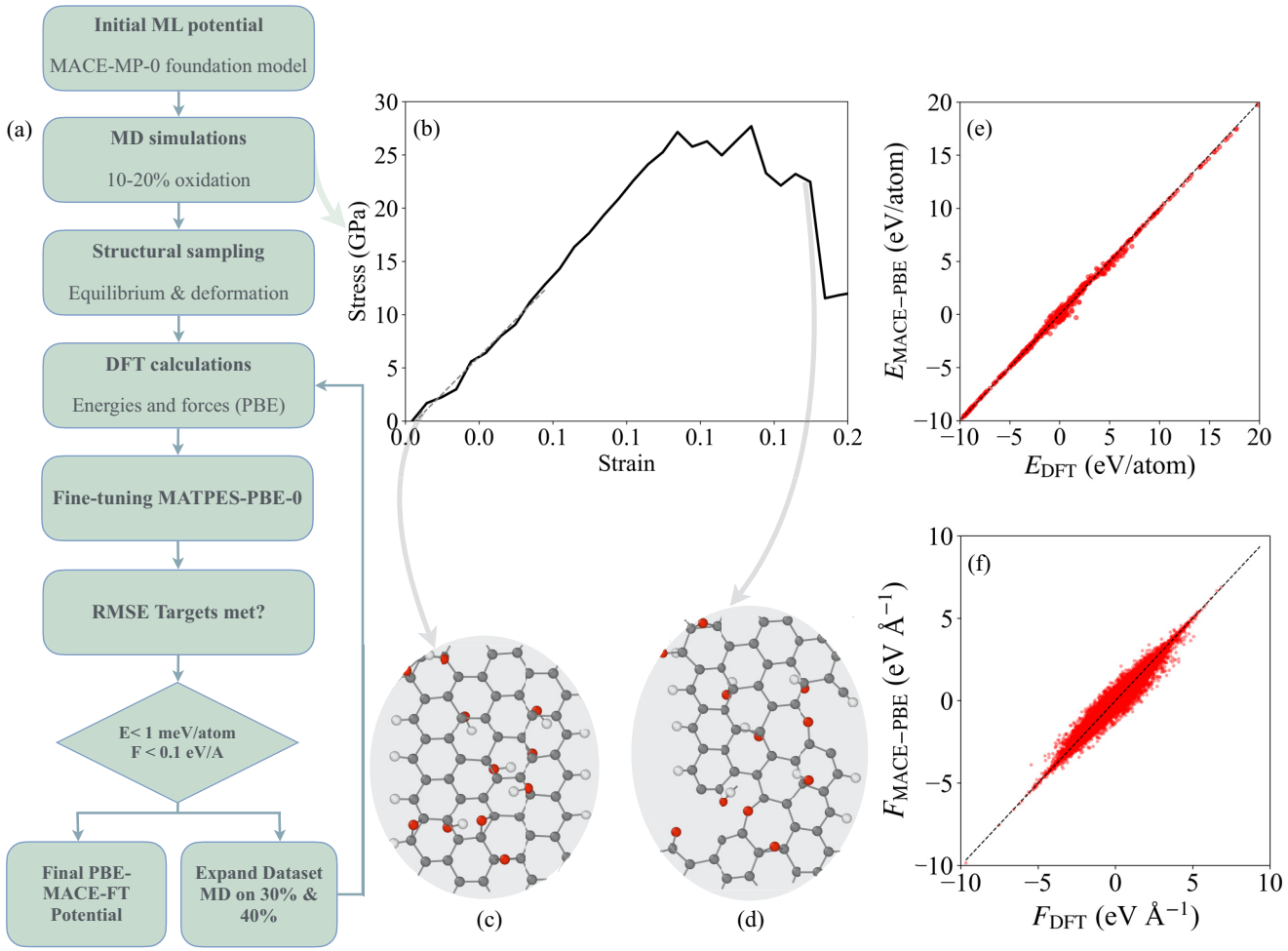


FIG. 1. Overview of the machine-learning potential development and validation workflow for GO. (a) Workflow used to construct the MLIP, including initial MD simulations with the MACE-MP-0 foundation model, structural sampling, DFT calculations for energy and force labeling, and iterative fine-tuning of the MACE model. (b) Representative stress-strain curve obtained from uniaxial tensile molecular dynamics simulations using the PBE-MACE-FT potential. (c), (d) Representative atomic configurations of GO nanoribbons illustrating the structure at the start of deformation and at the fracture point under uniaxial tensile loading. (e) Energy parity plot comparing DFT reference energies with those predicted by the PBE-MACE-FT model. (f) Force parity plot comparing DFT reference forces with the corresponding PBE-MACE-FT predictions.

by the instantaneous simulation-cell volume. The effective volume was defined using an assumed thickness of 0.75 nm for GO [56,57] and 0.335 nm for graphene [58]. Mechanical properties were extracted from the resulting stress-strain curves. The UTS corresponds to the maximum stress, while the associated strain defines the ultimate strain. The fracture strain is identified at the point of abrupt stress drop, and the Young's modulus is obtained from the linear elastic regime (up to 5% strain). To reduce short-time fluctuations in the stress-strain response, stress values sampled every 50 fs were averaged over consecutive intervals of 10 sampled points, corresponding to an averaging interval of 0.5 ps. The standard deviations calculated within these intervals quantify fluctuations along an individual deformation trajectory and do not represent statistical uncertainties across independently generated functional-group configurations. In this work, ductility is assessed from the extent of postpeak deformation in the stress-strain response, defined as the difference between the ultimate and fracture strain.

III. RESULTS

A. Development of the machine-learning interatomic potential

To construct a MLIP for GO, a training dataset consisting of atomic configurations and their corresponding energies and forces was generated from DFT calculations. The workflow used to construct the MLIP is illustrated in Fig. 1(a). Initial configurations were obtained from MD simulations of GO systems with relatively low oxidation levels (10%−20%) and an OH/O ratio of 0, 1, and hydroxyl-only functionalization. These simulations included energy minimization, thermal equilibration, and uniaxial deformation [see Fig. 1(b)], and were performed using the MACE-MP-0 foundation model [48]. From these simulations, representative configurations were selected to ensure structural diversity, including snapshots corresponding to different oxidation environments, functional-group distributions, and deformation regimes (elastic, plastic, and fracture). Representative snapshots are shown in Figs. 1(c) and 1(d). For each selected

configuration, reference energies and forces were computed using DFT with the PBE exchange-correlation functional.

Several available MACE foundation models were benchmarked against this initial DFT dataset by comparing the root-mean-square error (RMSE) in predicted energies and forces. Among the tested models, MATPES-PBE-0 [48] exhibited the lowest RMSE in both forces and energies (approximately 35 eV Å^{-1} for forces and 0.5 eV atom^{-1} for energies) and was therefore selected for fine-tuning. In the first training iteration, we fine-tuned the MATPES-PBE-0 foundation model using a dataset consisting of 993 training structures and 110 validation structures derived from the low-oxidation simulations described above. In a second iteration, the dataset was expanded by including additional DFT-labeled configurations obtained from MD simulations of higher-oxidation systems (30% and 40% oxidation, with OH/O ratios of 1 and 3), driven by the model fine-tuned during the first training iteration. This expansion increased the dataset to a total of 3318 training structures and 369 validation structures. Although the OH/O = 0.8 and 2.5 compositions used in the production simulations were not explicitly included in the fine-tuning dataset, the training data span a broad range of functional group compositions, from epoxy-only to hydroxyl-only systems, and include mixed systems with OH/O ratios of 1 and 3. This broad compositional coverage is expected to support the generalization of the model to intermediate OH/O ratios such as 0.8 and 2.5. The final fine-tuned MACE model (PBE-MACE-FT) achieves validation errors of approximately 2.2 meV atom^{-1} for energies and 60–70 meV Å^{-1} for forces, while remaining stable during molecular dynamics simulations under mechanical loading. Importantly, the larger GO systems used for the final validation were not included in the fine-tuning dataset, providing an explicit test of the model's transferability. The accuracy of the final MLIP is analyzed using the parity plots shown in Figs. 1(e) and 1(f).

B. Stress-strain behavior of GO nanoribbons

Following the development of the PBE-MACE-FT model, we now investigate its performance in describing the mechanical response of graphene and GO under uniaxial tensile deformation. For comparison, simulations are also performed using classical force fields. For systems where experimental data are available, we report and compare those values as well. To characterize the mechanical response, we extract key quantities from the stress-strain curves, including Young's modulus (E), UTS, ultimate strain (ε_u), and fracture strain (ε_f).

The simulation protocol, including system preparation, deformation procedure, and validation, is described in detail in the Methods section, Sec. II C.

As a first step, we discuss the results for pristine graphene that are reported in Table I. The Young's modulus and UTS calculated with the PBE-MACE-FT MLIP are in relative agreement with the experimental values [58]. From the comparison of the PBE-MACE-FT results with the ones obtained with the ReaxFF and AIREBO classical force fields [55], it does not emerge an improved description of the mechanical response of pristine graphene with respect to AIREBO, that is the reference model potential for CH systems, but is not transferable to oxygen containing systems. Indeed, while

TABLE I. Young's modulus and ultimate tensile stress of graphene sheets under uniaxial tensile deformation: comparison between experimental [58] and stress-strain MD simulations with different model potentials.

	Expt	AIREBO	ReaxFF	PBE-MACE-FT
E (GPa)	1000 ± 100	844 ± 1	1297 ± 3	872 ± 12
UTS (GPa)	130 ± 10	124 ± 1	143 ± 2	105 ± 1

ReaxFF significantly overestimates the Young's modulus, PBE-MACE-FT and AIREBO underestimate it somewhat. On the other hand, AIREBO predicts the UTS in relatively good agreement with experiment while PBE-MACE-FT and ReaxFF underestimates it by around 20% and 10%, respectively. These data tell us that PBE-MACE-FT MLIP is moderately transferable to pristine graphene, similarly to ReaxFF, even though it appears to perform much better in the linear response regime. In any case we should emphasize that the present PBE-MACE-FT MLIP has been obtained by fine tuning the MACE-MP-0 foundation model on GO systems only.

As mentioned, as AIREBO cannot be employed to study GO, in the rest of the article we will compare the PBE-MACE-FT performances only with ReaxFF ones.

Hence, we move to discuss the stress-strain curves for GO nanoribbons in simulations driven by the PBE-MACE-FT model and ReaxFF force field. Representative stress-strain curves for systems with 10% and 40% oxidation and different OH/O ratios are shown in Fig. 2, while other simulations are reported in Supplemental Material [59]. While at low oxidation PBE-MACE-FT and ReaxFF predict similar trends in ultimate strain [Figs. 2(a) and 2(b)], at higher oxidation the two models diverge significantly. For epoxy-rich systems [Fig. 2(c)], ReaxFF predicts significantly larger fracture strains, with deformation extending well beyond the failure point observed in PBE-MACE-FT. A similar discrepancy is observed in hydroxyl-rich systems [Fig. 2(d)], where both the ultimate strain and postpeak behavior differ substantially. In addition, ReaxFF systematically predicts larger mechanical values than PBE-MACE-FT, in some cases nearly two times larger. A quantitative comparison of Young's modulus, UTS, and fracture strain is presented in the following subsection.

C. Mechanical properties: Young's modulus, ultimate tensile stress, and ultimate strain

Having computed the stress-strain curves in the previous section, we now analyze the trends of the mechanical properties versus the oxidation level and the OH/O ratio. The Young's modulus, UTS, ultimate strain, and fracture strain are shown in Fig. 3 both for PBE-MACE-FT and ReaxFF.

We first focus on the Young's modulus and the UTS. According to the current literature, GO stiffness and strength are predicted to decrease with the oxidation level [33,35,36,38,60,61], reflecting the progressive disruption of the graphene sp^2 network as oxygen functional groups induce local sp^3 rehybridization, reducing the number of load-bearing C-C bonds [36,46,62].

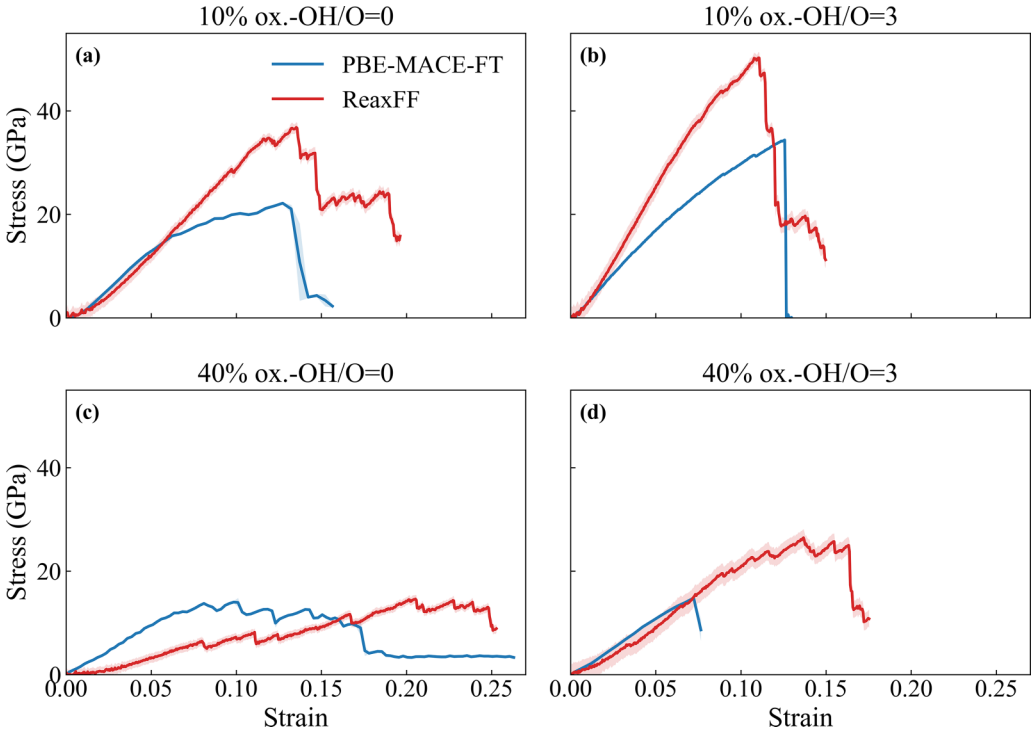


FIG. 2. Stress-strain response of GO nanoribbons under uniaxial tensile deformation predicted by the PBE-MACE-FT potential and the ReaxFF reactive force field. (a) 10% oxidation with epoxy-rich functionalization (OH/O = 0), (b) 10% oxidation with hydroxyl-rich functionalization (OH/O = 3), (c) 40% oxidation with epoxy-rich functionalization (OH/O = 0), and (d) 40% oxidation with hydroxyl-rich functionalization (OH/O = 3). Solid lines represent stress values averaged over 0.5 ps, while shaded regions indicate the corresponding fluctuations over the averaging window.

This behavior is captured by both potentials [Figs. 3(a), 3(b), 3(e), 3(f)], but with markedly different features.

ReaxFF model potential predicts a strong and irregular dependence of E and UTS on the oxidation level and the OH/O ratio, especially for the Young's modulus. At fixed oxidation levels, large variations are observed across different functional group compositions, often exceeding the changes induced by oxidation itself. For example, at 20% oxidation, the range spanned by the Young's modulus is $\Delta E \sim 280$ GPa for the explored OH/O ratio values, indicating that the elastic response might be greatly affected by the oxidation type.

A smaller, but still remarkable, spread is observed for the UTS, revealing that the same dependence survives also in the plastic regime. This "enhanced" sensitivity to functional group distribution at fixed oxidation levels, that was already reported in previous ReaxFF studies [33,60,63–66], is accompanied by a strong and irregular dependence of both E and UTS on the oxidation level, respectively spanning $\Delta_E \sim 460$ GPa and $\Delta_{\mathrm{UTS}} \sim 37$ GPa ranges for all the cases.

The usage of PBE-MACE-FT potential returns a different scenario, as both Young's modulus and UTS are primarily governed by the oxidation level, while the influence of the OH/O ratio remains comparatively moderate.

Although variations between different functional group compositions are present, the overall trends remain smooth and consistent across the investigated range. For instance, at 20% oxidation, the range spanned by the Young's modulus is markedly smaller $\Delta E \sim 60$ GPa for the explored OH/O ratio values. Also the ranges spanned by E and UTS are much smaller, respectively $\Delta_E \sim 180$ GPa and $\Delta_{\mathrm{UTS}} \sim 23$ GPa for all the cases. Moreover PBE-MACE-FT predicts lower values for both the Young's modulus and UTS, except perhaps some particular cases [see the Young's modulus for 10% oxidation and OH/O = 0 or OH/O = 1 in Figs. 3(a) and 3(e)].

This indicates that PBE-MACE-FT models predict that stiffness and strength are mainly governed by the extent of sp^2 network disruption rather than the ratio of epoxy to hydroxyl groups.

We now turn to analyze the dependence of the ultimate strain on the oxidation level and OH/O ratio [Figs. 3(c), 3(g)]. ReaxFF predicts a general tendency for ε_u to increase with the oxidation, particularly in epoxy-rich systems [Fig. 3(g)]. This trend is consistent with previous studies reporting an enhanced ductility with oxidation, especially in the presence of epoxy groups [33,35,36,62–64]. A similar increasing tendency is predicted for hydroxyl-rich systems. Recently, in epoxy-rich systems, the ultimate strain has been predicted to increase with oxidation up to ∼30%, followed by a slight decrease, resulting in a peak at intermediate oxidation [33]. The range spanned by the ReaxFF predicted ultimate strain is $\Delta_{\epsilon_u} \sim 0.13$ for all the cases treated, with a marked variation depending on the oxidation type.

The usage of the PBE-MACE-FT potential tells a different story: As shown in Fig. 3(c), the predicted ultimate strain depends weakly on the oxidation level and type as the range spanned for all the cases is $\Delta_{\varepsilon_u} \sim 0.05$, with an average $\varepsilon_u \sim 0.1$, lower than the one obtained with the ReaxFF model potential. At intermediate OH/O ratios, it remains nearly

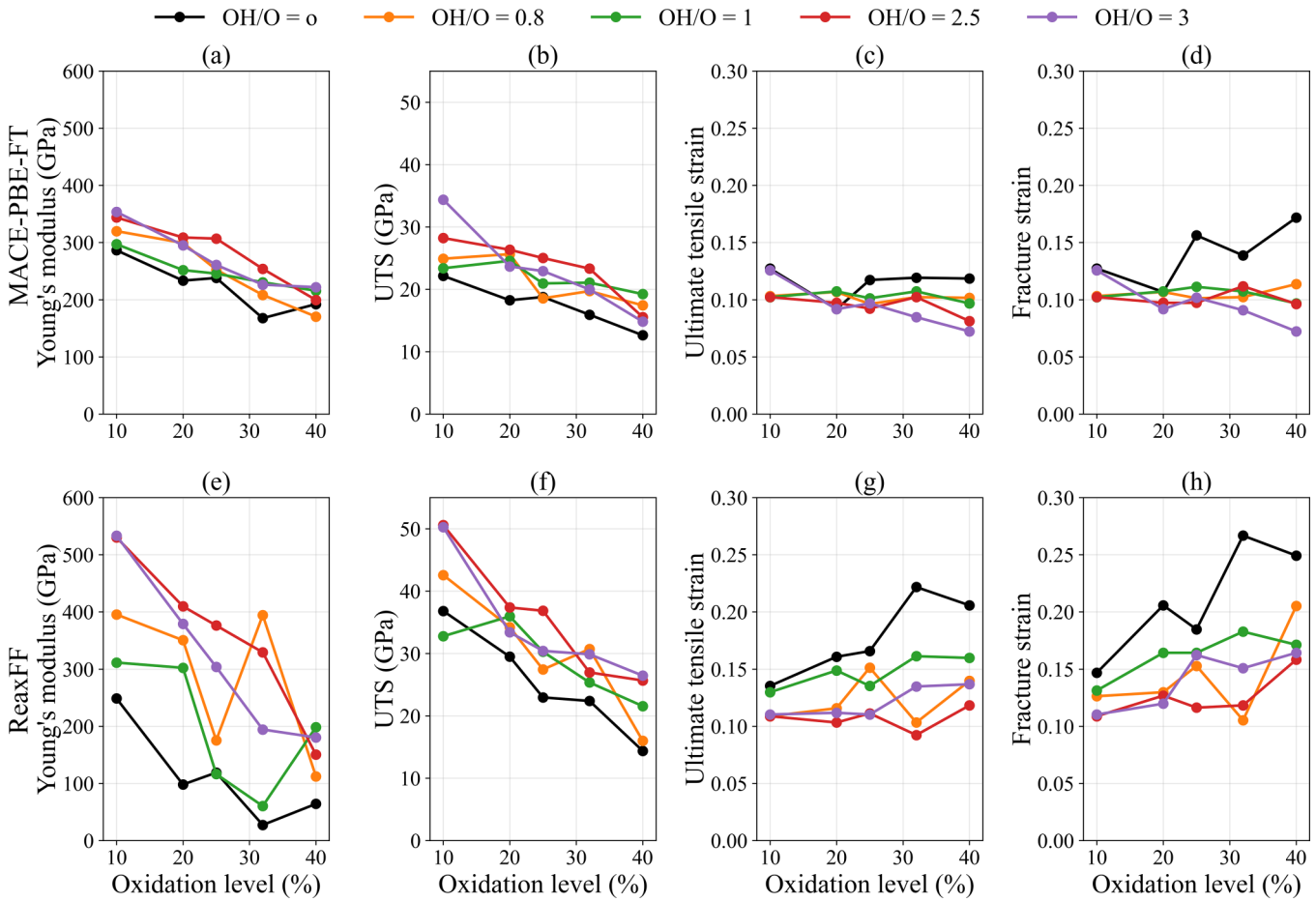


FIG. 3. Mechanical properties of GO as a function of oxidation level predicted by the PBE-MACE-FT potential (top row) and the ReaxFF reactive force field (bottom row). [(a),(e)] Young's modulus, [(b),(f)] UTS, and [(c),(g)] ultimate tensile strain and [(d),(h)] fracture strain. Different colored curves correspond to different hydroxyl-to-epoxy ratios (OH/O). Each data point corresponds to one single generated functional group configuration at the specified oxidation level and nominal OH/O ratio.

constant across the investigated oxidation range, indicating limited sensitivity to progressive functionalization. For epoxy-rich systems (OH/O = 0), a slight increase is observed beyond ∼20% oxidation, whereas hydroxyl-rich systems exhibit a gradual decrease. Overall, the variations remain small and the trends are smooth.

Generally speaking, the irregular trends found for E, UTS, and ε_u, and the much wider ranges spanned with varying oxidation level and type suggest that the ReaxFF model overestimates the influence of functional group distribution on the mechanical response, and that the mechanical properties appear "too reactive" to the increase of the oxidation level.

The usage of DFT-based MLIP depicts a new scenario characterized by a substantially lower sensitivity of the mechanical properties to the oxidation level and type.

To further assess the reliability of the PBE-MACE-FT model for mechanical properties, we compare our results with available experimental measurements. However, the comparison should be made with care as the experimental data are, quite often, affected by the variety of sample types and structures addressed.

Indeed, experimental studies report a broad range of Young's modulus values for graphene oxide, largely due to differences in oxidation level, functional group distribution, and sample preparation. For example, values around 250 ± 150 GPa have been reported for chemically derived graphene sheets [10], although these correspond to partially reduced graphene oxide.

However, more direct measurements on monolayer graphene oxide membranes are accessible from the literature and appear more suited to be compared to MD predictions: In this case, the experiments yield a narrower range for the Young's modulus of 207.6 ± 23.4 GPa [9] matching, with a very good agreement, the Young's modulus predicted by the PBE-MACE-FT potential for highly oxidized systems (32%–40%, ∼192–222 GPa), thus providing confidence in the reliability of the present PBE-MACE-FT MLIP.

D. Ductility, brittleness, and fracture mechanisms

To gain further insight into the ductility, brittleness, and failure behavior of GO, we now examine the fracture strain and the fracture mechanism, specifically their dependence on oxidation level and functional group composition. In the light of the findings discussed in the previous section, Sec. III C, one could expect a marked difference between the predictions of PBE-MACE-FT and ReaxFF on the GO brittle/ductile behavior, as ReaxFF overestimates the mechanical response

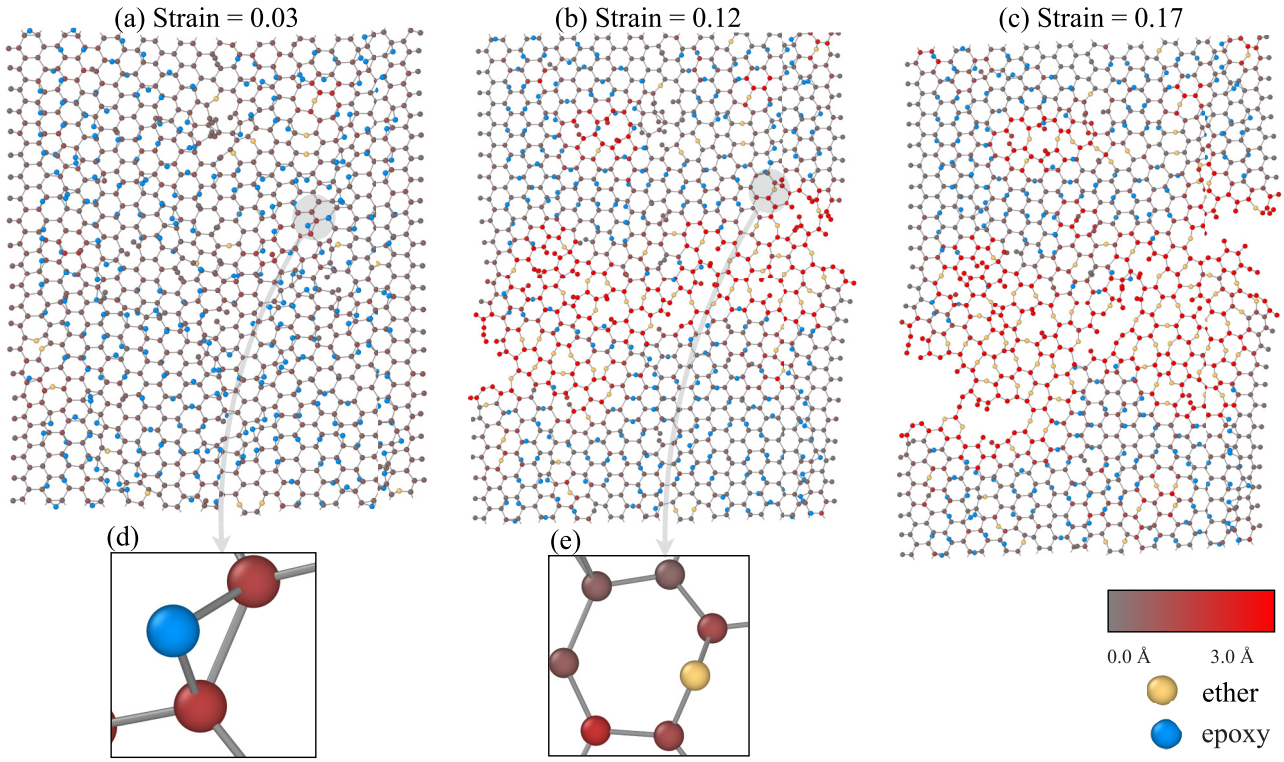


FIG. 4. Nonaffine displacement maps of GO with 40% oxidation and epoxy-rich functionalization (OH/O = 0) under uniaxial tensile loading, obtained from PBE-MACE-FT simulations. (a)–(c) Evolution of the GO nanoribbon at increasing strain levels: $\varepsilon = 0.03$, 0.12, and 0.17 (fracture strain). At low strain, deformation is relatively homogeneous, while at higher strain it becomes strongly localized. Atoms are colored according to their local nonaffine displacement magnitude (color scale), highlighting regions of intense structural rearrangement. (d) Magnified view of a representative epoxy configuration prior to transformation. (e) Corresponding region after transformation, showing the formation of an ether configuration. The spatial correlation between regions of high nonaffine displacement and ether formation indicates that epoxy-to-ether transformation contributes to localized strain accommodation prior to fracture.

to oxidation level and type in both the elastic and plastic regimes.

Indeed, by examining the fracture strain ε_f [Figs. 3(d), 3(h)] relative to the ultimate strain ε_u, we see that ReaxFF systematically predicts an increase of ε_f with the oxidation for all OH/O ratios, indicating an overall increase in ductility that is largely independent of the functional group composition. According to ReaxFF, the ductile character of GO is particularly marked for epoxy-rich systems (OH/O = 0) that consistently exhibit higher fracture strains compared to other functional group compositions.

The scenario depicted by the PBE-MACE-FT potential is more varied and realistic [Figs. 3(c) and 3(d)]. At low oxidation levels (up to ∼20%), the response is predominantly brittle, with the ultimate and fracture strain coinciding for all OH/O ratios. Beyond this threshold, ductility becomes more pronounced and shows a clear dependence on the functional group composition. In epoxy-rich systems (OH/O = 0), a clear increase in ductility is observed with increasing oxidation, with the difference between fracture and ultimate strain reaching values above ∼0.04 at high oxidation levels. In contrast, systems with intermediate OH/O ratios (0.8, 1, and 2.5) remain largely brittle across the entire oxidation range, exhibiting only minimal postyield deformation ($\Delta\varepsilon = \varepsilon_f - \varepsilon_u < 0.01$). Hydroxyl-rich systems (OH/O = 3) show a limited increase in ductility at high oxidation, which remains significantly smaller than that of epoxy-rich systems.

Another relevant aspect concerns the absolute magnitude of the fracture strain. The values predicted by PBE-MACE-FT remain consistently lower than that of pristine graphene (∼0.19), reflecting the progressive weakening of the carbon network induced by oxygen functionalization. In contrast, ReaxFF predicts higher fracture strain values in some cases (e.g., around 30% oxidation), suggesting an overestimation of ductility by the empirical force field.

To better understand the fracture mechanism, we analyze the atomistic processes underlying deformation and failure. We first focus on the epoxy-to-ether transformation, which is a known key mechanism underlying ductility in graphene oxide [33,46]. We focus on the deformation of a GO nanoribbon with 40% oxidation and epoxy-rich functionalization (OH/O = 0), shown in Fig. 4, in a simulation driven by PBE-MACE-FT. At low strain, the oxygen atom in the shaded region of Fig. 4(a) forms an epoxy group bonded to two neighboring carbon atoms, as depicted in Fig. 4(d). At higher strain, this epoxy group transforms into a bridging ether configuration near the fracture site [see Fig. 4(e)]. To elucidate the effects of the epoxy-to-ether transformation we analyze the nonaffine displacements for this system. In Fig. 4(a) we show that at low strain ($\varepsilon = 0.03$), deformation is limited and relatively homogeneous across the lattice. Instead,

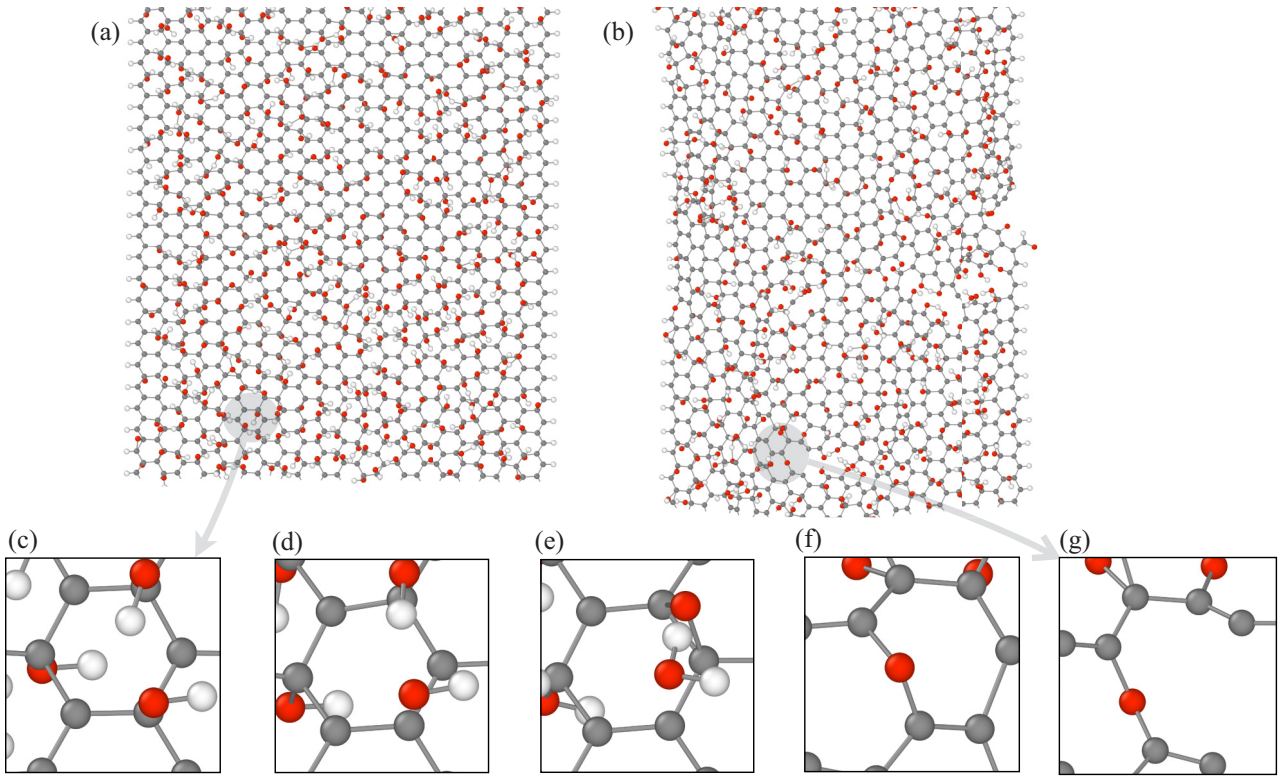


FIG. 5. Representative deformation and local structural transformations in GO, 40% (OH/O = 2.5) under tensile loading in MACE-PBE-FT. (a), (b) GO nanoribbon before deformation and at the fracture point, respectively. (c), (g) magnified views of a representative region highlighting the sequence of atomistic transformations. (c) Initial configuration prior to deformation. (d) Detachment of a hydroxyl group from the carbon lattice. (e) Formation of a water molecule (H_2O) through hydrogen transfer, accompanied by the reformation of an epoxy group. (f) Subsequent epoxy-to-ether transformation at $\varepsilon = 0.08$, where the epoxy group rearranges into a bridging C-O-C configuration. (g) Final configuration near fracture [corresponding to (b)].

close to fracture ($\varepsilon = 0.12$), and at the fracture point ($\varepsilon = 0.17$) the deformation becomes strongly localized, as shown in Figs. 4(b) and 4(c), respectively. We can also observe in Figs. 4(b) and 4(c) that the regions with high nonaffine displacement are spatially correlated with ether-rich areas. Together, these observations indicate that the epoxy-to-ether transformation plays a key role in accommodating strain. In regions of high local deformation, epoxy groups rearrange into ether configurations, acting as a stress-relief mechanism and delaying crack propagation. This mechanism is consistent with previous studies, where the epoxy-to-ether transformation has been identified as a primary source of ductility in GO [46].

While the epoxy-to-ether transformation is observed in all systems containing epoxy groups, it is not clear whether its effect on ductility is the same across different oxidation levels and functional group compositions. To address this, we analyze the evolution of ether formation during deformation following the approach of Ref. [33]. Our analysis shows that a rapid epoxy-to-ether conversion alone is not sufficient to delay fracture, which explains the absence of significant ductility in low-oxidation epoxy-rich systems (below ∼20%). Instead, ductility correlates more consistently with the net ether content, defined as the product of the ether fraction and the oxidation level, i.e., as the percentage of ethers relative to carbons. Systems exhibiting enhanced ductility reach net ether contents above ∼12%, whereas systems with limited ductility fall within ∼3% to 7%, and brittle systems remain below ∼2%. For more information, see Supplemental Material [59].

Up to this point, we have focused on the role of epoxy functional groups. We now turn to the effect of hydroxyl groups on the ductility and fracture behavior of GO. In simulations performed with PBE-MACE-FT, particularly for systems with oxidation levels above ∼25% and OH/O ratios greater than 1, we observe hydroxyl detachment accompanied by the formation of water molecules. This behavior is illustrated in Fig. 5 for GO with 40% oxidation and OH/O = 2.5. A representative local configuration containing two neighboring hydroxyl groups (vicinal diols) is shown in Fig. 5(c), which corresponds to the shaded area of Fig. 5(a). This local configuration transforms according to the reaction path shown in Figs. 5(c)–5(g). One of the hydroxyl groups detaches from the carbon ring, as shown in Fig. 5(d), followed by the formation of a water molecule, while the remaining oxygen atom reconfigures into an epoxy group [Fig. 5(e)]. We refer to this sequence as a dehydration process, which can occur during energy minimization, equilibration, or deformation. At later stages of deformation, around $\varepsilon = 0.08$ and near fracture [Fig. 5(f)], this epoxy group further transforms into an ether configuration. In Fig. 5(g) we show the same ether configuration at the fracture point.

This hydroxyl detachment mechanism is consistent with previous theoretical studies reporting the intrinsic instability of vicinal diols in GO [67]. In our simulations, however, the process proceeds further through proton transfer and water formation, introducing a pathway for the creation of new epoxy groups. Its occurrence increases with both oxidation level and hydroxyl content, as higher concentrations favor unstable hydroxyl arrangements.

As a representative example, in the 40% oxidation system with OH/O = 3, the OH/O ratio decreases from ∼3, in the initial structure to ∼2.0 after NPT equilibration and to ∼1.8 near fracture, while the amount of formed water reaches approximately 8%. In contrast, for the 25% oxidation system with OH/O = 3, the OH/O ratio is ∼2.9 after equilibration, ∼2.7 at fracture, and the water formation remains below 1%.

We want to emphasize that the above dehydration process is only captured by the PBE-MACE-FT models as it was completely absent in the stress strain dynamics modeled with the ReaxFF force field. Since all systems were simulated at the same temperature and strain rate, while dehydration becomes substantially more pronounced at high oxidation levels and OH/O ratios, the observed differences are primarily associated with the local chemical composition rather than with differences in the simulation conditions. Moreover, a substantial decrease in the OH/O ratio is already observed during NPT equilibration, before the tensile deformation begins, indicating that the dehydration process is not exclusively induced by the applied strain or the relatively high MD strain rate. Nevertheless, the strain rate may influence the extent and kinetics of dehydration during deformation. The results reported here were obtained within the PBE approximation to the exchange-correlation functional. The dehydration process observed here involves local covalent-bond rearrangements and proton transfer between neighboring hydroxyl groups, whose energetics are primarily governed by the local chemical bonding environment. Dispersion interactions may nevertheless affect the relative stability and spatial arrangement of neighboring functional groups and, consequently, the hydrogen-bond network involved in proton transfer. The use of other exchange-correlation approximations, including meta-GGA, dispersion-corrected, and hybrid functionals, may therefore quantitatively affect these energetics. However, previous benchmark calculations have shown that adding D3 or Tkatchenko-Scheffler dispersion corrections to PBE has only a minor effect on proton-transfer barriers [68]. Therefore, while the quantitative energetics may depend on the choice of functional, the qualitative picture of the dehydration mechanism reported here is not expected to be substantially altered.

IV. CONCLUSION

In this work, we systematically investigated the effect of oxidation level and hydroxyl-to-epoxy ratio on the mechanical response of GO using both a classical force field (ReaxFF) and a fine-tuned machine learning potential (PBE-MACE-FT). Our study spans a broad range of oxidation levels (10%–40%) and functional group compositions, covering conditions close to experimental observations while extending to regimes—particularly high OH/O ratios—that remain largely unexplored in previous studies.

Consistent with prior literature, both models predict a decrease in Young's modulus and UTS with increasing oxidation, reflecting the progressive disruption of the sp^2 carbon network due to sp^3 rehybridization. However, significant differences emerge in the sensitivity to functional group composition. The PBE-MACE-FT results show a relatively weak dependence on the OH/O ratio, with smooth and consistent trends across all oxidation levels. In contrast, ReaxFF exhibits a strong and irregular dependence on functional group distribution, systematically overestimating both Young's modulus and UTS and amplifying variations at fixed oxidation.

The effect of oxidation and functionalization on ductility reveals a more complex behavior. Contrary to the common assumption that increasing oxidation enhances ductility in epoxy-rich systems through the epoxy-to-ether transformation, our results show that this trend does not hold at low oxidation levels, where the response remains predominantly brittle. Overall, oxidation has a weaker and less systematic influence on ductility compared to its clear impact on stiffness and strength. While ReaxFF reproduces qualitatively similar trends at low oxidation, it predicts an artificial increase in ductility at higher oxidation levels, indicating limitations in its description of fracture mechanisms.

At the atomistic level, PBE-MACE-FT provides additional insight into the mechanisms governing fracture. While the epoxy-to-ether transformation remains a key strain-relief mechanism in epoxy-rich systems, we identify a competing pathway in hydroxyl-rich environments involving hydroxyl detachment and water formation. This process can occur already during minimization, equilibration, and deformation, and becomes more pronounced at higher oxidation levels and OH/O ratios. These observations show a clear correlation between the increasing activity of the hydroxyl detachment pathway and the reduced ductility of highly oxidized OH-rich systems. Unlike the epoxy-to-ether transformation, which preserves oxygen within the lattice as a bridging group and facilitates strain accommodation, hydroxyl detachment and water formation involve stronger local bond rearrangements and are associated with increased structural disorder. As a result, this competing mechanism promotes earlier failure and contributes to the decrease in fracture strain with increasing oxidation. This behavior is not captured by ReaxFF as it is unable to describe hydroxyl detachment and water formation.

ACKNOWLEDGMENTS

G.Z. and S.S.F. wish to acknowledge the partial support by the Next Generation EU program, Mission 4, Component 2, CUP B33C22000710006, Project iEntrance@ENL-Infrastructure for Energy Transition, and Circular Economy @EURONANOLAB. We are also grateful for the computational resources provided on the Hyperion cluster at the Donostia International Physics Center (DIPC) and on MareNostrum 5 ACC at the Barcelona Supercomputing Center, granted through the Spanish Supercomputing Network

(RES) allocation 2025-3-0045. P.M.P. acknowledges funding from the Ramón y Cajal programme (Grant No. RYC2024-049807-I) funded by MICIU/AEI/10.13039/501100011033 and by the European Social Fund Plus (FSE+).

DATA AVAILABILITY

The simulation scripts, fine-tuned machine-learning interatomic potential, and representative input structures associated with this study are openly available in Zenodo [69].

[1] I. Chowdhury, M. C. Duch, N. D. Mansukhani, M. C. Hersam, and D. Bouchard, Colloidal properties and stability of graphene oxide nanomaterials in the aquatic environment, Environ. Sci. Technol. **47**, 6288 (2013).

[2] S. Eigler, S. Grimm, F. Hof, and A. Hirsch, Graphene oxide: A stable carbon framework for functionalization, J. Mater. Chem. A **1**, 11559 (2013).

[3] S. Kim, S. Zhou, Y. Hu, M. Acik, Y. J. Chabal, C. Berger, W. de Heer, A. Bongiorno, and E. Riedo, Room-temperature metastability of multilayer graphene oxide films, Nat. Mater. **11**, 544 (2012).

[4] P. V. Kumar, M. Bernardi, and J. C. Grossman, The impact of functionalization on the stability, work function, and photoluminescence of reduced graphene oxide, ACS Nano **7**, 1638 (2013).

[5] S. Park, K. S. Lee, G. Bozoklu, W. Cai, S. B. T. Nguyen, and R. S. Ruoff, Graphene oxide papers modified by divalent ions—Enhancing mechanical properties *via* chemical cross-linking, ACS Nano **2**, 572 (2008).

[6] Z. Xu, H. Sun, X. Zhao, and C. Gao, Ultrastrong fibers assembled from giant graphene oxide sheets, Adv. Mater. **25**, 188 (2013).

[7] C. Xiang, C. C. Young, X. Wang, Z. Yan, C.-C. Hwang, G. Cerioti, J. Lin, J. Kono, M. Pasquali, and J. M. Tour, Large flake graphene oxide fibers with unconventional 100% knot efficiency and highly aligned small flake graphene oxide fibers, Adv. Mater. **25**, 4592 (2013).

[8] C. Wang, M. D. Frogley, G. Cinque, L. Q. Liu, and A. H. Barber, Deformation and failure mechanisms in graphene oxide paper using *in situ* nanomechanical tensile testing, Carbon **63**, 471 (2013).

[9] J. W. Suk, R. D. Piner, J. An, and R. S. Ruoff, Mechanical properties of monolayer graphene oxide, ACS Nano **4**, 6557 (2010).

[10] C. Gómez-Navarro, M. Burghard, and K. Kern, Elastic properties of chemically derived single graphene sheets, Nano Lett. **8**, 2045 (2008).

[11] A. Nourbakhsh, M. Cantoro, T. Vosch, G. Pourtois, F. Clemente, M. H. van der Veen, J. Hofkens, M. M. Heyns, S. De Gendt, and B. F. Sels, Bandgap opening in oxygen plasma-treated graphene, Nanotechnology **21**, 435203 (2010).

[12] P. Johari and V. B. Shenoy, Modulating optical properties of graphene oxide: Role of prominent functional groups, ACS Nano **5**, 7640 (2011).

[13] Y. Gao, L. Q. Liu, S. Z. Zu, K. Peng, D. Zhou, B. H. Han, and Z. Zhang, The effect of interlayer adhesion on the mechanical behaviors of macroscopic graphene oxide papers, ACS Nano **5**, 2134 (2011).

[14] Q. He, S. Wu, S. Gao, X. Cao, Z. Yin, H. Li, P. Chen, and H. Zhang, Transparent, flexible, all-reduced graphene oxide thin film transistors, ACS Nano **5**, 5038 (2011).

[15] G. Eda, G. Fanchini, and M. Chhowalla, Large-area ultrathin films of reduced graphene oxide as a transparent and flexible electronic material, Nat. Nanotechnol. **3**, 270 (2008).

[16] M. B. Askari and P. Salarizadeh, State-of-the-art review on reduced graphene oxide for supercapacitor electrode applications, Results Eng. **28**, 107429 (2025).

[17] L. S. Sundar and M. W. Ashraf, Synthesis and characterization methods of graphene oxide nanomaterial for biomedical and toxicity applications: A comprehensive review, Inorg. Chem. Commun. **174**, 113936 (2025).

[18] X. Huang, W. Zhao, F. Khalilov, and N. Xu, Graphene oxide: Preparation and medical research, Materials **18**, 2855 (2025).

[19] A. Pandey, J. Singh, M. Singh, G. Singh, A. S. Parmar, and S. Chaudhary, Graphene oxide/polylactic acid composites with enhanced electrical and mechanical properties for 3D-printing materials, J. Mol. Struct. **1329**, 141420 (2025).

[20] Z. Y. Hu, Y. Wan, Y. J. Duan, Y. H. Shi, C. P. Gu, R. Ma, J. J. Dong, and D. Cui, A review of the impact of graphene oxide on cement composites, Nanomaterials **15**, 216 (2025).

[21] A. Buchsteiner, A. Lerf, and J. Pieper, Water dynamics in graphite oxide investigated with neutron scattering, J. Phys. Chem. B **110**, 22328 (2006).

[22] C. Botas, P. Álvarez, C. Blanco, R. Santamaría, M. Granda, P. Ares, F. Rodríguez-Reinoso, and R. Menéndez, The effect of the parent graphite on the structure of graphene oxide, Carbon **50**, 275 (2012).

[23] P. Feicht, R. Siegel, H. Thurn, J. W. Neubauer, M. Seuss, T. Szabó, A. V. Talyzin, C. E. Halbig, S. Eigler, D. A. Kunz, A. Fery, G. Papastavrou, J. Senker, and J. Breu, Systematic evaluation of different types of graphene oxide in respect to variations in their in-plane modulus, Carbon **114**, 700 (2017).

[24] T. Cassagneau, F. Guérin, and J. H. Fendler, Preparation and characterization of ultrathin films layer-by-layer self-assembled from graphite oxide nanoplatelets and polymers, Langmuir **16**, 7318 (2000).

[25] S. Zhou and A. Bongiorno, Origin of the chemical and kinetic stability of graphene oxide, Sci. Rep. **3**, 2484 (2013).

[26] C. Hontoria-Lucas, A. J. López-Peinado, J. de D. López-González, M. L. Rojas-Cervantes, and R. M. Martín-Aranda, Study of oxygen-containing groups in a series of graphite oxides: Physical and chemical characterization, Carbon **33**, 1585 (1995).

[27] H. V. Kumar, S. J. Woltornist, and D. H. Adamson, Fractionation and characterization of graphene oxide by oxidation extent through emulsion stabilization, Carbon **98**, 491 (2016).

[28] A. M. Dimiev and J. M. Tour, Mechanism of graphene oxide formation, ACS Nano **8**, 3060 (2014).

[29] S. Saxena, T. A. Tyson, and E. Negusse, Investigation of the local structure of graphene oxide, J. Phys. Chem. Lett. **1**, 3433 (2010).

[30] S. You, S. M. Luzan, T. Szabó, and A. V. Talyzin, Effect of synthesis method on solvation and exfoliation of graphite oxide, Carbon **52**, 171 (2013).

[31] D. A. Dikin, S. Stankovich, E. J. Zimney, R. D. Piner, G. H. B. Dommett, G. Evmenenko, S. B. T. Nguyen, and R. S. Ruoff, Preparation and characterization of graphene oxide paper, Nature (London) **448**, 457 (2007).

[32] K. Chenoweth, A. C. T. van Duin, and W. A. Goddard, ReaxFF reactive force field for molecular dynamics simulations of hydrocarbon oxidation, J. Phys. Chem. A **112**, 1040 (2008).

[33] S. S. Fashtali and G. Zollo, Chemical and oxidation level dependence of mechanical response to uniaxial tensile stress in mono-layered GO nano-flakes, Comput. Mater. Sci. **258**, 114107 (2025).

[34] M. Nasr Esfahani, S. Shahbeigi, and M. Jabbari, Effect of oxygen configurations on the mechanical properties of graphene oxide, J. Appl. Phys. **132**, 174302 (2022).

[35] X. Zhang, S. Liu, H. Liu, J. Zhang, and X. Yang, Molecular dynamics simulation of the mechanical properties of multilayer graphene oxide nanosheets, RSC Adv. **7**, 55005 (2017).

[36] Y. Sun, X. Tang, H. Bao, Z. Yang, and F. Ma, The effects of hydroxide and epoxide functional groups on the mechanical properties of graphene oxide and its failure mechanism by molecular dynamics simulations, RSC Adv. **10**, 29610 (2020).

[37] X. Liu and Q. Yang, Molecular dynamic simulation of mechanical behaviour of RGO produced by thermal reduction method, Micro Nano Lett. **12**, 638 (2017).

[38] Y. Bu, K. Li, F. Guo, Z. Liang, and J. Zhang, Mechanical behavior and failure mechanism of multilayer graphene oxides with various oxygen contents and functional types: A ReaxFF molecular dynamics simulation, Appl. Surf. Sci. **606**, 154920 (2022).

[39] M. Feng, Y. Wang, and K. H. Luo, Atomistic insight into enhanced thermal decomposition of energetic material on graphene oxide, Proc. Combust. Inst. **39**, 5687 (2023).

[40] Z. Yang and Y. Sun, Tension dynamics of graphene oxide and peculiar change of yield strain, Appl. Nanosci. **10**, 1825 (2020).

[41] B. B. Sharma, A. Kedare, G. Muralidharan, and A. Govind Rajan, Understanding the effects of surface and edge functionalization on the mechanical properties of graphene and graphene oxide, ChemPhysChem **26**, e202400919 (2025).

[42] Q. Chen, I. M. De Cachinho Cordeiro, W. Yang, A. C. Y. Yuen, T. B. Y. Chen, W. Wang, W. Yang, G. H. Yeoh, and R. K. K. Yuen, Exploring graphdiyne: Dynamic characterisation of the surface oxidation mechanisms via ReaxFF-MD and experiments, Carbon **232**, 119793 (2025).

[43] B. D. Jensen, K. E. Wise, and G. M. Odegard, Simulation of the elastic and ultimate tensile properties of diamond, graphene, carbon nanotubes, and amorphous carbon using a revised ReaxFF parametrization, J. Phys. Chem. A **119**, 9710 (2015).

[44] A. Kabylda, B. Mortazavi, X. Zhuang, and A. Tkatchenko, Mechanical properties of nanoporous graphenes: Transferability of graph machine-learned force fields compared to local and reactive potentials, Adv. Funct. Mater. **35**, 2417891 (2025).

[45] C. Cao, M. Daly, C. V. Singh, Y. Sun, and T. Filleter, High strength measurement of monolayer graphene oxide, Carbon **81**, 497 (2015).

[46] X. Wei, L. Mao, R. A. Soler-Crespo, J. T. Paci, J. Huang, S. B. T. Nguyen, and H. D. Espinosa, Plasticity and ductility in graphene oxide through a mechanochemically induced damage tolerance mechanism, Nat. Commun. **6**, 8029 (2015).

[47] J. P. Perdew, K. Burke, and M. Ernzerhof, Generalized gradient approximation made simple, Phys. Rev. Lett. **77**, 3865 (1996).

[48] I. Batatia, P. Benner, Y. Chiang, A. M. Elena, D. P. Kovács, J. Riebesell, X. R. Advincula, M. Asta, M. Avaylon, W. J. Baldwin, F. Berger, N. Bernstein, A. Bhowmik, F. Bigi, S. M. Blau, V. Cărare, M. Ceriotti, S. Chong, J. P. Darby, S. De, *et al.*, A foundation model for atomistic materials chemistry, J. Chem. Phys. **163**, 184110 (2025).

[49] P. Giannozzi, S. Baroni, N. Bonini, M. Calandra, R. Car, C. Cavazzoni, D. Ceresoli, G. L. Chiarotti, M. Cococcioni, I. Dabo, A. Dal Corso, S. de Gironcoli, S. Fabris, G. Fratesi, R. Gebauer, U. Gerstmann, C. Gougoussis, A. Kokalj, M. Lazzeri, L. Martin-Samos, *et al.*, QUANTUM ESPRESSO: A modular and open-source software project for quantum simulations of materials, J. Phys.: Condens. Matter **21**, 395502 (2009).

[50] P. Giannozzi, O. Andreussi, T. Brumme, O. Bunau, M. Buongiorno Nardelli, M. Calandra, R. Car, C. Cavazzoni, D. Ceresoli, M. Cococcioni, N. Colonna, I. Carnimeo, A. Dal Corso, S. de Gironcoli, P. Delugas, R. A. DiStasio Jr, A. Ferretti, A. Floris, G. Fratesi, G. Fugallo, *et al.*, Advanced capabilities for materials modelling with QUANTUM ESPRESSO, J. Phys.: Condens. Matter **29**, 465901 (2017).

[51] A. Dal Corso, Pseudopotentials periodic table: From H to Pu, Comput. Mater. Sci. **95**, 337 (2014).

[52] A. Lerf, H. He, M. Forster, and J. Klinowski, Structure of graphite oxide revisited, J. Phys. Chem. B **102**, 4477 (1998).

[53] A. Hjorth Larsen, J. Jørgen Mortensen, J. Blomqvist, I. E. Castelli, R. Christensen, M. Dułak, J. Friis, M. N. Groves, B. Hammer, C. Hargus, E. D. Hermes, P. C. Jennings, P. Bjerre Jensen, J. Kermode, J. R. Kitchin, E. Leonhard Kolsbjerg, J. Kubal, K. Kaasbjerg, S. Lysgaard, J. B. Maronsson, *et al.*, The atomic simulation environment—a Python library for working with atoms, J. Phys.: Condens. Matter **29**, 273002 (2017).

[54] A. P. Thompson, H. M. Aktulga, R. Berger, D. S. Bolintineanu, W. M. Brown, P. S. Crozier, P. J. in 't Veld, A. Kohlmeyer, S. G. Moore, T. D. Nguyen, R. Shan, M. J. Stevens, J. Tranchida, C. Trott, and S. J. Plimpton, LAMMPS - a flexible simulation tool for particle-based materials modeling at the atomic, meso, and continuum scales, Comput. Phys. Commun. **271**, 108171 (2022).

[55] S. J. Stuart, A. B. Tutein, and J. A. Harrison, A reactive potential for hydrocarbons with intermolecular interactions, J. Chem. Phys. **112**, 6472 (2000).

[56] B. Rezania, N. Severin, A. V. Talyzin, and J. P. Rabe, Hydration of bilayered graphene oxide, Nano Lett. **14**, 3993 (2014).

[57] C. M. Chen, Q. H. Yang, Y. Yang, W. Lv, Y. Wen, P. X. Hou, M. Wang, and H. M. Cheng, Self-assembled free-standing graphite oxide membrane, Adv. Mater. **21**, 3007 (2009).

[58] C. Lee, X. Wei, J. W. Kysar, and J. Hone, Measurement of the elastic properties and intrinsic strength of monolayer graphene, Science **321**, 385 (2008).

[59] See Supplemental Material at http://link.aps.org/supplemental/10.1103/vwr6-mt41 for the complete set of stress-strain curves for all investigated oxidation levels and OH/O ratios, and additional analysis of the evolution of ether configurations during deformation.

[60] C. Wang, Q. Peng, J. Wu, X. He, L. Tong, Q. Luo, J. Li, S. Moody, H. Liu, R. Wang, S. Du, and Y. Li, Mechanical characteristics of individual multi-layer graphene-oxide sheets under direct tensile loading, Carbon **80**, 279 (2014).

[61] Z. El-Machachi, B. Cheng, and V. L. Deringer, Mechanical properties of graphene oxide from machine-learning-driven simulations, Chem. Commun. **61**, 11405 (2025).

[62] R. A. Soler-Crespo, W. Gao, P. Xiao, X. Wei, J. T. Paci, G. Henkelman, and H. D. Espinosa, Engineering the mechanical properties of monolayer graphene oxide at the atomic level, J. Phys. Chem. Lett. **7**, 2702 (2016).

[63] M. R. T. Bidhendi and K. Behdinan, High-velocity transverse impact of monolayer graphene oxide by a molecular dynamics study, Comput. Mater. Sci. **216**, 111881 (2023).

[64] A. Khoei and M. Khorrami, Mechanical properties of graphene oxide: A molecular dynamics study, Fuller. Nanotub. Carbon Nano. **24**, 594 (2016).

[65] M. Tavakol, A. Montazeri, S. H. Aboutalebi, and R. Asgari, Mechanical properties of graphene oxide: The impact of functional groups, Appl. Surf. Sci. **525**, 146554 (2020).

[66] A. Verma and A. Parashar, Molecular dynamics based simulations to study failure morphology of hydroxyl and epoxide functionalised graphene, Comput. Mater. Sci. **143**, 15 (2018).

[67] R. J. W. E. Lahaye, H. K. Jeong, C. Y. Park, and Y. H. Lee, Density functional theory study of graphite oxide for different oxidation levels, Phys. Rev. B **79**, 125435 (2009).

[68] S. Seyedraoufi and K. Berland, Improved proton-transfer barriers with van der Waals density functionals: Role of repulsive non-local correlation, J. Chem. Phys. **156**, 244106 (2022).

[69] S. S. Fashtali, Graphene oxide mechanics with machine-learning interatomic potentials, Zenodo, Version 1.0.0 (2026), software, doi: 10.5281/zenodo.23262750.